To appear in *Vehicle System Dynamics*
Vol. 00, No. 00, Month 20XX, 1–20

A free-trajectory quasi-steady-state optimal-control method for minimum lap-time of race vehicles

M. Veneri and M. Massaro*

Department of Industrial Engineering, University of Padova,
Via Venezia 1, 35131 Padova, Italy

(*Received 00 Month 20XX; accepted 00 Month 20XX*)

Minimum lap time problems are usually solved employing quasi-steady-state models on a predetermined (fixed) trajectory or employing dynamic models on a free (i.e. not predetermined) trajectory. This work describes a third approach, where the minimum-lap-time problem is solved using quasi-steady-state models and free trajectory. The method builds upon g-g maps that can either be derived numerically or experimentally. Such g-g-speed surfaces can either represent the performance of a car or a motorcycle. Both a double-track car model and a motorcycle model are employed as examples of applications. The effect of the free-trajectory vs. fixed-trajectory assumption is also discussed.

Keywords: minimum lap-time; free-trajectory; fixed-trajectory; g-g map; cars; motorcycles.

1. Introduction

The investigation of minimum-time manoeuvring has become a widely used approach to improve the performance of road vehicles, especially race ones. Early attempts to solve minimum-lap-time problems dates back to the late 1950s [1], while in the late 1980s minimum-time simulations of sections of the Paul Ricard circuit were presented [2].

There are a variety of minimum-lap-time problems: they may have a free or predetermined trajectory, and may use dynamic or quasi-steady-state models. In the case of free-trajectory problems, the race line is determined by the optimisation solver, while for fixed-trajectory problems, the race line is determined from track data or from previous free-trajectory solutions. As a general rule, fixed-trajectory problems are faster to solve, since a lower number of variables is involved.

The most widespread combinations reported in the literature to solve minimum-lap-time problems are basically two: quasi-steady-state (QSS) models with predetermined trajectory, see e.g. [2–10], and dynamic models with free-trajectory, see e.g. [11–25]. The former approaches usually involve the computation of the well-known g-g map of the vehicle at different speed (g-g-speed surface), together with the determination of the corner apexes on the trajectory (i.e. the points at which the vehicle has maximum lateral acceleration). The latter approaches usually involve the solution of a nonlinear-optimal-control problem (OCP), which may be solved either with direct or indirect methods [26, 27].

*Corresponding author. Email: matteo.massaro@unipd.it

The focus of the current work is to devise a free-trajectory method employing QSS models for minimum-lap time of cars and motorcycles. The method builds upon the g-g diagrams, which are commonly computed to analyse the vehicle performance, and retains the advantage of determining the optimal trajectory of the road vehicle. Numerical models of very high complexity can be employed, since all their features (e.g. tyre limits, power limits, aerodynamic drag and downforce, suspensions, etc.) are summarised by the related g-g diagrams, and do not affect the complexity of the OCP that needs to be solved. The method allows to employ even experimental g-g diagrams in place of numerical ones, and is suitable for application to both cars and motorcycles.

The work is organised as follows. In Section 2 the parametrisation of the g-g-speed surface is explained, for subsequent implementation in the OCP. In Section 3 the optimal control problem is built upon the g-g diagrams, for the computation of the minimum-lap time and optimal trajectory. Remarks on differences with fixed-trajectory approaches (both OCP and 'apex-finding') are included. In Section 4 two examples of applications are shown: the first considers a 415 kW race car and the second a 180 kW race motorcycle. The related g-g-speed surfaces are computed, and the OCP is solved on the Adria International Raceway (Italy).

2. g-g diagram

The calculation of the g-g diagrams is a well-known method for assessing the performance of vehicles, see e.g. [5, 6, 10]. A typical car g-g diagram is shown in Fig. 1 (left). The boundaries of such diagram are found maximising the performance of the vehicle at different speeds V, in order to find the maximum and minimum longitudinal acceleration a_x, for a given lateral acceleration a_y.

At 'low' speeds, the g-g envelope is limited by the tyre-friction characteristics, both in acceleration and in braking. The boundary is reached when one or more tyres saturate. At 'high' speeds the effect of aerodynamics becomes dominant: the maximum acceleration is now limited by the power limit (the higher the speed, the lower the maximum acceleration available for traction), whereas in braking the drag force contributes to increasing the braking performance. In the case of motorcycles, the g-g envelope is further limited when front or rear tyre normal load reduces to zero, i.e. when the front or rear tyre lifts from the ground (see Section 4.2).

Given its typical shape, the g-g diagram can be conveniently parametrised using polar

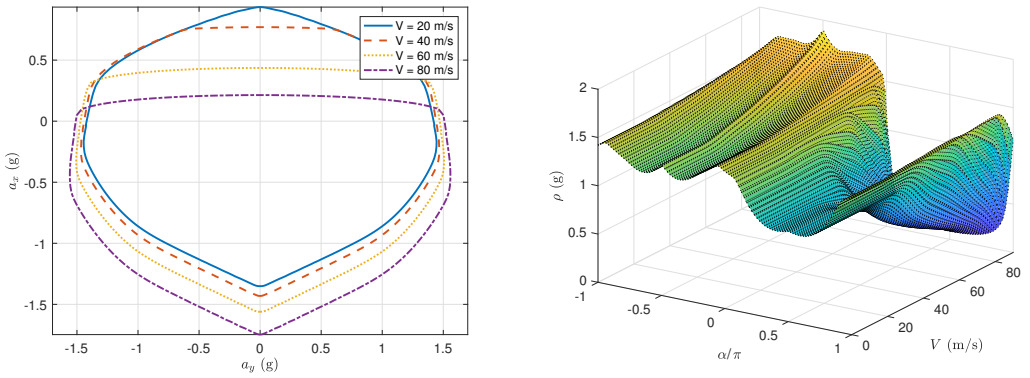

Figure 1.: g-g map of a car at different speeds (left) and related adherence radius as a function of the orientation angle and vehicle speed (right).

coordinates; this will also make it easier to introduce the g-g constraint in the minimum-time-optimisation problem (see Section 3):

$$\rho = \sqrt{\left(\frac{a_x}{g}\right)^2 + \left(\frac{a_y}{g}\right)^2}, \tag{1}$$

$$\alpha = \arctan\left(\frac{a_x}{a_y}\right). \tag{2}$$

where ρ is the adherence radius, and α is the related orientation. The values of the adherence radius at different speed are then interpolated by means of splines, to give the following surface

$$\rho = \rho(\alpha, V), \tag{3}$$

which is a function of the polar orientation α and the speed V; see Fig. 1 (right).

The method presented remains valid when using both numerically calculated and empirically measured g-g diagrams. Two examples of application of the g-g-speed surfaces are given for a race car model in Section 4.1, and a race motorcycle model in Section 4.2.

3. Optimal control problem

3.1. *Free-trajectory OCP*

The method combines a free-trajectory minimum-time OCP with the QSS approach adopted for the generation of g-g diagrams. The model used in the OCP consists of a three-degrees-of-freedom model, which is constrained to move within the road borders, while satisfying the limits of the g-g-speed surface. All the complexity of the vehicle, e.g. tyre nonlinearities, aerodynamics, etc., are included in the g-g map.

The model state variables $\mathbf{x}$ are the absolute velocity V along the trajectory, the lateral position n with respect to the road center line, and the relative orientation χ with respect to the tangent to the center line (see Fig. 2):

$$\mathbf{x} = \{V,\, n,\, \chi\}^T. \tag{4}$$

The related state equations (in the time domain) are

$$\dot{V} = a_x, \tag{5}$$

$$\dot{n} = \sin(\chi)\, V, \tag{6}$$

$$\dot{\chi} = a_y/V - \dot{\theta}, \tag{7}$$

where a_x and a_y are the longitudinal and lateral accelerations, $\dot{\theta}$ is the derivative of the orientation of the road centre line with respect to the absolute reference frame. The first term on the right-hand side of (7) arises from the equation $a_y = \dot{\psi}V = \Omega V$, where $\dot{\psi} = \Omega$ is the yaw rate. The control vector $\mathbf{u}$ of the OCP consists of the longitudinal and lateral accelerations

$$\mathbf{u} = \{a_x,\, a_y\}^T. \tag{8}$$

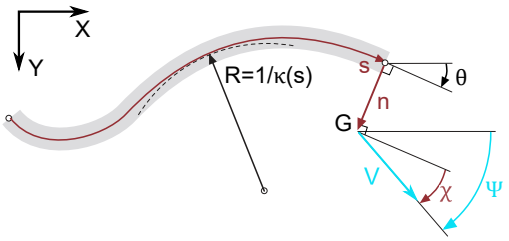

Figure 2.: Road model: G represents the vehicle.

The model can be conveniently rewritten in the space domain

$$\mathbf{x}' = \frac{d\mathbf{x}}{ds} = \frac{\dot{\mathbf{x}}}{\dot{s}}, \tag{9}$$

using the curvilinear coordinate s along the center line (see Fig. 2)

$$\dot{s} = \frac{\cos(\chi)}{1 - n\kappa} V, \tag{10}$$

where κ is the curvature of the road center line.

The target $\mathcal{L}$ of the OCP is the manoeuvre time, which can be computed from the speed along the center line as follows

$$\mathcal{L} = \int dt = \int \frac{1}{\dot{s}} ds. \tag{11}$$

Finally, the vehicle is constrained to move within the road borders

$$-r_{wl} \leq n \leq r_{wr}, \tag{12}$$

where r_{wl} and r_{wr} represent the left and right road limits, and to satisfy the g-g envelope

$$\rho \leq \rho_{\max}, \tag{13}$$

where $\rho_{\max} = \rho_{\max}(\alpha, V)$ is the maximum value of the adherence radius ρ (given by (1)) at the current orientation α (given by (2)) and speed V.

The OCP can be solved numerically using direct or indirect methods [26]. It is noted that the resulting OCP is simple, although the underlying vehicle model can be complex.

3.2. *Remarks on fixed-trajectory methods*

The more standard minimum-time problem with fixed-trajectory can be obtained from the OCP approach in Section 3.1, when removing (6), (7) and (12), i.e. when only (5) and (13) are retained, using the curvilinear abscissa along the race line (instead of along the centreline) as the independent variable.

Alternatively, the minimum-time problem with fixed-trajectory can be solved without any OCP approach, using the widespread methods reported e.g. in [2–10]. In this case, the corner apexes need be identified first: at each apex, where the trajectory curvature is maximum, the vehicle is assumed to have maximum lateral acceleration. Before the apex the vehicle is braking along the g-g envelope, while after the apex the tyres are

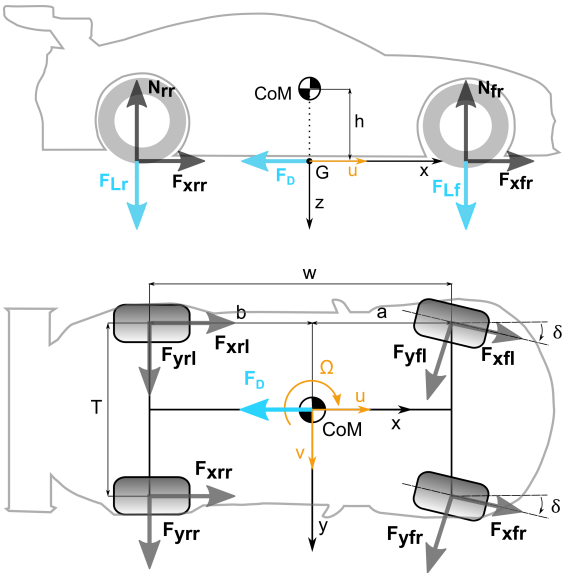

Figure 3.: Car model.

engaged with traction forces in order to keep the vehicle along the g-g envelope. The speed profiles between two apexes (acceleration out of turn i and deceleration into turn $i+1$) are then connected at their intersection point. Sometimes it is assumed that at each apex the longitudinal acceleration is zero, which is a slightly different condition (when compared with the maximum lateral acceleration condition): in this scenario, after the apex the vehicle is accelerating.

In the case an OCP approach is selected, the apexes are automatically identified by the optimiser and no assumption on their locations need be made.

Further considerations are included in Sec. 4.1.4, where the optimisation of a vehicle parameter is carried using the three methods (free-trajectory OCP, fixed-trajectory OCP and fixed-trajectory apex-finding).

4. Examples of application

The free-trajectory quasi-steady-state method introduced in Section 3.1 is now applied both to a car model and a motorcycle model, in order to show its main features. The procedure for both the car and the motorcycle is the same. First, the g-g maps for each vehicle are obtained, at different speeds. Second, all g-g diagrams (for each vehicle) are combined to give the adherence radius surface in (3): biquintic splines have been used in these examples (bilinear splines have shown not smooth enough to avoid numerical problems). Third, the OCP problem is run on a given track: in this case the Adria International Raceway (Italy). A direct solution method is employed to solve the OCP [26, 28]. Automatic differentiation is used to speed-up the computation time [29].

4.1. *Car model*

A double-track car model is employed to generate the g-g map shown in Fig. 1, with the baseline parameters and related meaning given in Tab. 1. The wheel-steering angle δ is assumed small, the roll, pitch and bounce degrees of freedom are neglected, together with the suspension travels. Similar models have been used in [20, 21, 27, 30, 31]. The

steady-state equations of the vehicle are given by

$$ma_x = (F_{xfl} + F_{xfr} + F_{xrl} + F_{xrr}) - (F_{yfl} + F_{yfr})\,\delta - F_D, \tag{14}$$

$$ma_y = (F_{yfl} + F_{yfr} + F_{yrl} + F_{yrr}) + (F_{xfl} + F_{xfr})\,\delta, \tag{15}$$

$$0 = mg + F_{Lf} + F_{Lr} - N_{fl} - N_{fr} - N_{rl} - N_{rr}, \tag{16}$$

$$ma_y h = \frac{T}{2}(N_{fl} - N_{fr} + N_{rl} - N_{rr}), \tag{17}$$

$$ma_x\, h = aF_{Lf} - bF_{Lr} - a(N_{fl} + N_{fr}) + b(N_{rl} + N_{rr}), \tag{18}$$

$$\begin{aligned} 0 = {} & \frac{T}{2}\,(F_{yfl} - F_{yfr})\,\delta - a\,(F_{xfl} + F_{xfr})\,\delta + \frac{T}{2}\,(-F_{xfl} + F_{xfr} - F_{xrl} + F_{xrr}) + \\ & - a\,(F_{yfl} + F_{yfr}) + b\,(F_{yrl} + F_{yrr})\,, \end{aligned} \tag{19}$$

where the first three equations represent the force balance along the longitudinal, lateral and vertical direction respectively, while the latter three equations represent the moment balance around the roll, pitch and yaw axes through the projection of the center of mass on the ground. In (14) and (19), the longitudinal acceleration is $a_x = \dot{u} - \Omega v$, where u and v are the longitudinal and lateral velocity of the vehicle respectively ($V = \sqrt{u^2 + v^2}$ is the total velocity), while Ω is the yaw rate. In (15) and (18), the lateral acceleration is $a_y = \Omega u$. The aerodynamics forces consist of the drag force F_D, the front F_{Lf} and rear F_{Lr} downforces. They are applied on the road plane (see Fig. 3), and are given by

$$F_D = \frac{1}{2}\,\rho_a\, C_D A\, u^2, \qquad F_{Lf} = \frac{1}{2}\,\rho_a\, C_{Lf} A\, u^2, \qquad F_{Lr} = \frac{1}{2}\,\rho_a\, C_{Lr} A\, u^2. \tag{20}$$

The tyre longitudinal and lateral forces are given by F_{xij} and F_{yij} respectively, where $i = f, r$ (front, rear) and $j = l, r$ (left, right). The tyre forces are computed employing the Magic Formula with theoretical slips [32]:

$$F_x = N\,\frac{\sigma_x}{\sigma}\,D_x \sin\{C_x\,\arctan\,[B_x\,\sigma - E_x\,(B_x\,\sigma - \arctan(B_x\,\sigma))]\}, \tag{21}$$

$$F_y = N\,\frac{\sigma_y}{\sigma}\,D_y \sin\{C_y\,\arctan[B_y\,\sigma - E_y\,(B_y\,\sigma - \arctan(B_y\,\sigma))]\}, \tag{22}$$

with

$$\sigma_x = \frac{\kappa}{1+\kappa}, \quad \sigma_y = \frac{\tan(\lambda)}{1+\kappa}, \quad \sigma = \sqrt{\sigma_x^2 + \sigma_y^2}, \tag{23}$$

where the theoretical slips σ_x, σ_y and σ are computed from the longitudinal and lateral (practical) slips κ and λ [32]. The lateral slips λ_{ij} of the current model are

$$\lambda_{fl} = \delta - \frac{v + \Omega a}{u + \frac{T}{2}\Omega}, \qquad \lambda_{fr} = \delta - \frac{v + \Omega a}{u - \frac{T}{2}\Omega}, \tag{24}$$

$$\lambda_{rl} = -\frac{v - \Omega b}{u + \frac{T}{2}\Omega}, \qquad \lambda_{rr} = -\frac{v - \Omega b}{u - \frac{T}{2}\Omega}. \tag{25}$$

The longitudinal slip will be an input to the model. Finally, B, C, D and E are the

Pacejka's coefficients, which are herein expressed in the simplified form introduced in [23]. The purpose is to avoid the full Magic Formula formulation, while retaining some of its key features, namely load dependent friction coefficients, load-dependent position of the peak of the force vs. slip curves, and load dependent cornering stiffness per unit load. The coefficients are

$$K_x = B_x\, C_x\, D_x = N\, pK_{x1} \exp(pK_{x3}\, df_z), \tag{26}$$

$$E_x = pE_{x1}, \tag{27}$$

$$D_x = (pD_{x1} + pD_{x2}\, df_z)\, \lambda_{\mu,x}, \tag{28}$$

$$C_x = pC_{x1}, \tag{29}$$

$$B_x = \frac{K_x}{C_x\, D_x\, N}, \tag{30}$$

$$K_y = N_0\, pK_{y1}\, \sin\left(2\, \arctan \frac{N}{pK_{y2}\, N_0}\right), \tag{31}$$

$$E_y = pE_{y1}, \tag{32}$$

$$D_y = (pD_{y1} + pD_{y2}\, df_z)\, \lambda_{\mu,y}, \tag{33}$$

$$C_y = pC_{y1}, \tag{34}$$

$$B_y = \frac{K_y}{C_y\, D_y\, N}, \tag{35}$$

where $df_z = \frac{N-N_0}{N_0}$ and N_0 is a reference load. The dataset of tyre parameters is given in Tab. 1.

The tyre normal forces are given by N_{ij}, where again $i = f, r$ and $j = l, r$ (see Fig. 3), and are computed from the system consisting of (16), (17) and (18), with the roll stiffness balance

$$ma_y \frac{h}{T}\xi = \frac{N_{fl} - N_{fr}}{2}, \tag{36}$$

where $\xi = \frac{K_{\phi f}}{K_{\phi f}+K_{\phi r}}$ is the roll stiffness ratio, $K_{\phi f}$ is the front-axle roll stiffness, and $K_{\phi r}$ is the rear-axle roll stiffness.

The total driving force F_x is split between the rear and front axle according to the distribution factor k_t, under the open-differential assumption:

$$F_{xfl} = \frac{(1-k_t)F_x}{2}, \qquad F_{xfr} = \frac{(1-k_t)F_x}{2}, \tag{37}$$

$$F_{xrl} = \frac{k_t F_x}{2}, \qquad F_{xrr} = \frac{k_t F_x}{2}. \tag{38}$$

During acceleration $k_t = 1$ for rear-wheel-drive (RWD) vehicles, $k_t = 0$ for front-wheel-drive (FWD) vehicles, and $0 < k_t < 1$ for all-wheel-drive (AWD) vehicles. During braking the distribution factor is given by

$$k_t = \frac{1}{1+\gamma}, \qquad \gamma = \frac{F_{xfl} + F_{xfr}}{F_{xrl} + F_{xrr}}, \tag{39}$$

where γ is the brake ratio, which is here defined as the ratio between the front and rear longitudinal tyre forces – the switch between the value of k_t in acceleration and the value of k_t in braking is implemented through an approximation of a piecewise function, in order to avoid numerical issues.

Summarising, given the longitudinal velocity u, the longitudinal acceleration a_x, and the lateral acceleration a_y, the vehicle trim can be computed by solving the steady-state equations (14)-(19), the roll balance (36), the brake ratio (39), the open-differential conditions $F_{xfl} = F_{xfr}$ and $F_{xrl} = F_{xrr}$, for the four normal loads N_{ij}, the steering angle δ, the four tyre longitudinal slips κ_{ij}, and the lateral velocity v.

The g-g maps of the car are obtained by means of an nonlinear optimisation problem, in which the target is to maximise the adherence radius (1), subject to the steady-state equations (14)-(19) and (36)-(38). The optimiser seeks to maximise such radius for a set of absolute velocities and orientations. In this case the velocity V takes five values (between 20 and 90 m/s), while the orientation α takes 90 values (between $-\pi/2$ and $\pi/2$). The g-g diagram is assumed symmetric with respect to the zero lateral acceleration (vertical) axis.

The optimiser IPOPT [33] has been employed for the solution of the problem, together with the automatic differentiation tool ADiGator [29], which generates the derivatives required by the optimiser. A proper guess is important for the solution. Since the g-g diagram is computed step-by-step, the guess of each point (except the first one) is based on the solution at the previous step, unless the residuals of the constraints evaluated at the new step are above a given threshold. In the latter case a new guess is generated by exploiting a combination of possible slips, steering angles, and adherence radii around the previously converged solution.

The first g-g points to be computed are usually those at $a_y = 0$ or $a_x = 0$, because they can be easily solved, while coupled conditions (where both longitudinal and lateral accelerations are involved) are usually more challenging. The cost function is

$$\mathcal{J} = -\rho, \tag{40}$$

where ρ is the adherence radius.

Additional constraints are included to account for the limited steering angle

$$|\delta| \leq \delta_{\max}, \tag{41}$$

and for the limited engine power

$$F_x u \leq P_{\max}, \tag{42}$$

where F_x is the total driving force.

Finally, multiple solutions exist when it comes to negotiating a turn [34]. The aim in the present example is to avoid the solutions characterized by very large slip angles, e.g. power-slide manoeuvres and skidding. Therefore, constraints are added to prevent the tyre-slips from exceeding the values at which the longitudinal and lateral forces attain their maxima

$$\kappa \leq \kappa_{\max}, \qquad \lambda \leq \lambda_{\max}. \tag{43}$$

The maximum longitudinal slip $\kappa_{\max}$ depends on the normal load and the lateral slip angle, while the maximum lateral slip angle $\lambda_{\max}$ depends on the normal load and the

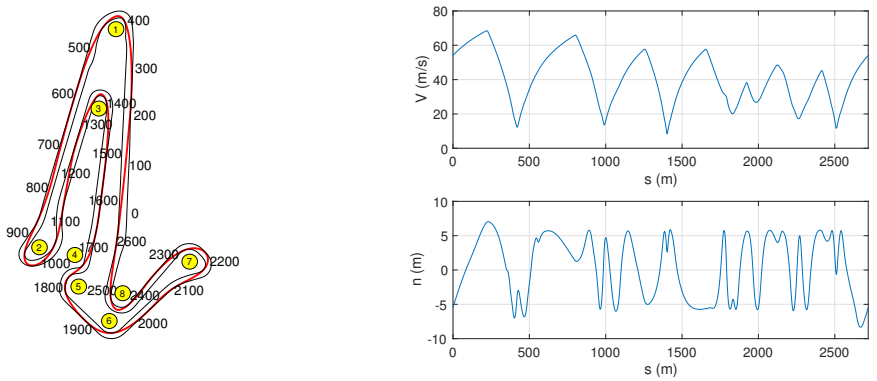

Figure 4.: Baseline car configuration. Trajectory on the Adria International Raceway (left), with corner numbers and distance (curvilinear abscissa s) from the start/finish line. Speed V (top-right) and lateral position n (bottom-right) along the curvilinear coordinate.

longitudinal slip. Again, a number of normal loads is defined (from 0 to 12000 N), and interpolated using bilinear splines.

4.1.1. Baseline simulation

The race line obtained with the free-trajectory OCP is shown in Fig. 4 (left) using the baseline parameters of the RWD car reported in Tab. 1. The vehicle runs anticlockwise on the Adria International Raceway (Italy), which is characterised by a total length of 2702 m, and eight turns mainly paced at speeds below 15 m/s. The minimum speed is 8.5 m/s at turn 3. The top speed is 68 m/s and is reached on the pit straight; see Fig. 4 (right). The resulting optimum lap time is 75.451 s. The lateral position n shows how the car moves between the inner and outer border of the track, whose width is variable between 11 m and 17 m; see Fig. 4 (right).

As expected, when solving the fixed-trajectory OCP (see Section 3.2), using the race line obtained with the free-trajectory OCP, the lap time is nearly identical (difference of 0.01%). When solving the lap-time problem with the fixed-trajectory apex-finding approach (see Section 3.2), using the race line obtained with the free-trajectory OCP, the lap time is again nearly identical (difference of 0.01%).

The three results are coherent, although the problems are discretised using differently spaced mesh points along the track centre line. The mesh points of the OCP solutions are unevenly spaced (in the range 0.1-10 m) and result from the solution of the optimisation problem[1], while the apex-finding approach has a 0.1 m equally spaced mesh. See Sec. 4.1.5 for further details on the computation implications of the different methods.

4.1.2. Effect of friction on the race-line

The coefficients $\lambda_{\mu,x}$ and $\lambda_{\mu,y}$ in (28) and (33) are halved, in order to simulate a low-friction condition, e.g. very wet vs. dry condition. In the baseline friction scenario, the lap time is 75.451 s, while in the low friction scenario the lap time increases to 102.727 s. The low-friction-OCP results are compared to the baseline simulation (i.e. baseline friction)

[1]The unevenly spaced mesh is obtained through the hp mesh refinement scheme described in [28], which simultaneously varies the mesh size (h) and the order (p) of the approximating polynomials.

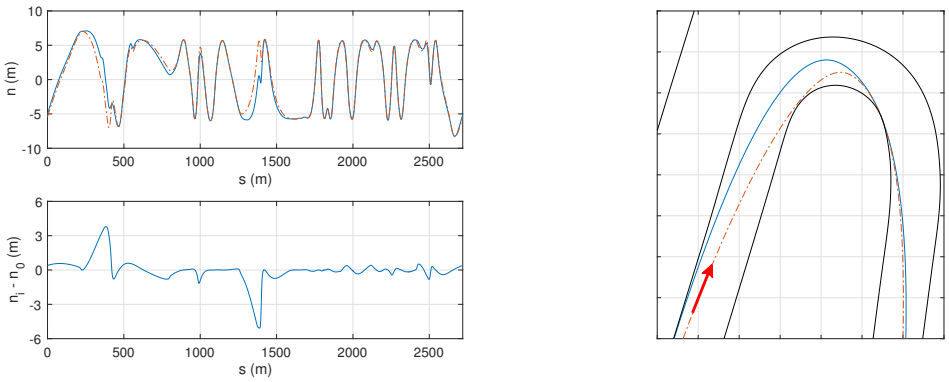

Figure 5.: Lateral position n at different road-tyre friction (top-left) and lateral position difference with respect to the baseline configuration (bottom-left). Magnified view of turn 3, with different race lines (right). Baseline (dot-dash), low friction (solid).

in Fig. 5. The race line differs significantly in the two scenarios, in particular in the tight corners. When the vehicle enters turn 1 (300-500 m), the optimal lateral position n in the low-friction scenario is 4 m closer to the outer border with respect to the baseline friction scenario. The same behaviour is observed in turn 3 (1300-1500 m).

4.1.3. Effect of brake ratio on the race line

A small change in the brake ratio γ, defined in (39), can give a quite different behaviour of the vehicle during braking. Three γ configurations are chosen for the present investigation: the baseline configuration (A), a configuration with γ increased by 10% (B), and a configuration with γ reduced by 10% (C). The lateral position n of the three configurations is compared in Fig. 6. In general, the A and C configurations have an opposite behaviour during corners. The baseline brake ratio value γ_0 is reported in Tab. 1. The lap time is 75.451 s for vehicle A, 75.040 s for vehicle B and 75.844 s for vehicle C. At turn 1 (300-500 m), vehicle B approaches the corner closer to the outer border with respect to vehicle A, adopts a tighter trajectory during cornering, and moves towards the outer border again at the exit of the corner. The difference between the lateral position n of vehicle B and A, in this case, is 0.5 m. Vehicle C, instead, runs tighter to the inner border before the turn, goes larger during the turn, and exits the turn closer to the inner border. At turn 2 (900-1100 m) the behaviour is similar to turn 1. At turn 3 (1300-1500 m), vehicle B employs a wider race line both while entering and exiting the corner, while vehicle C employs the opposite strategy, with a trajectory closer to the inner side of the corner. Vehicle B has a maximum lateral position difference of 1.3 m, with respect to the baseline trajectory (A), while leaving the turn.

4.1.4. Effect of race-line on the roll stiffness optimum

The roll stiffness ratio ξ in (36) affects the lateral load transfer on each axle, while the total lateral load transfer remains the same. The effect of such parameter on the race line is shown in Fig. 7 for three configurations: the baseline vehicle (A), the vehicle with ξ increased by 20% (B), and the vehicle with ξ reduced by 20% (C). The baseline roll stiffness ratio ξ_0 is reported in Tab. 1. At turn 1 (300-500 m) and 2 (900-1100 m), vehicle B reaches the apex travelling on a race line closer to the inner kerb, and exits the corner with a larger trajectory with respect to vehicle A (baseline). At turn 3 (1300-1500 m),

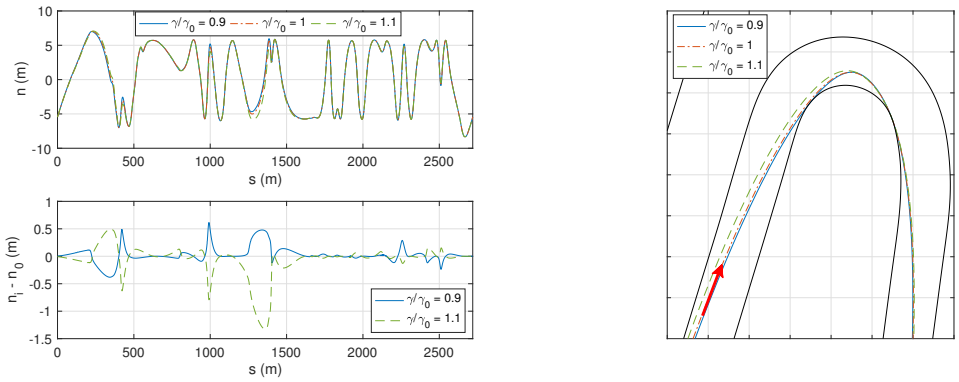

Figure 6.: Lateral position of n at different brake ratios γ (top-left) and lateral position difference with respect to the baseline configuration (bottom-left). Magnified view of turn 3, with different race lines (right). Baseline (dot-dash), brake ratio -10% (solid), brake ratio +10% (dashed).

vehicle B drives closer to the outer border during the corner and then closer to the inner border in the exit phase. At turn 8 (2100-2300 m) the maximum difference of lateral position is observed (1.2 m): again vehicle B drives the corner closer to the inner kerb. In each case, vehicle C adopts an opposite strategy with respect to vehicle B.

A parameter optimisation is run in order to find the roll ratio that gives the minimum lap time. Both the baseline adherence and the low adherence cases are considered. The optimisation is carried out by employing the free-trajectory OCP, the fixed-trajectory OCP, and the fixed-trajectory apex-finding method. The fixed-trajectory methods are run using the race line obtained with the corresponding free-trajectory OCP. The three methods give the same optimum, both in the baseline-friction ($\xi/\xi_0 = 1.6$) and low-friction ($\xi/\xi_0 = 1.7$) scenario (see Fig. 8). Indeed, as explained in Sec. 4.1.1, the three methods give roughly the same lap time, once the (same) race line is given.

A deeper investigation shows that increasing the roll stiffness ratio is detrimental for the maximum achievable lateral acceleration, since the load transfer on the front axle is already large in the baseline configuration. However, while simultaneously braking (or

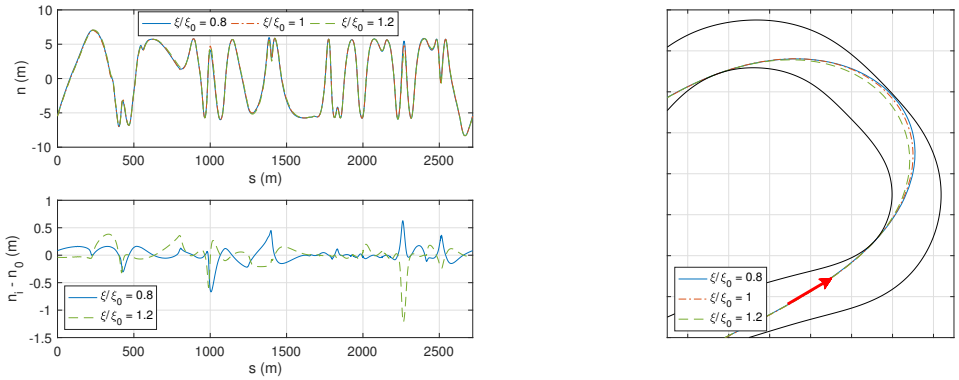

Figure 7.: Lateral position n at different roll stiffness ratios ξ (top-left) and lateral position difference with respect to the baseline configuration (bottom-left). Magnified view of turn 8, with different race lines. Baseline (dot-dash), roll stiffness ratio -20% (solid), roll stiffness ratio +20% (dashed).

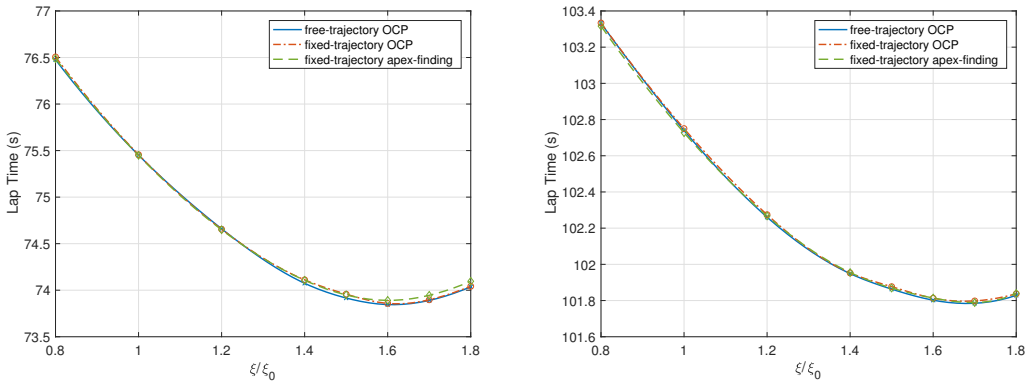

Figure 8.: Lap time versus the normalised roll-ratio parameter ξ/ξ_0 for baseline friction (left) and low friction (right), using the free-trajectory OCP method (solid), the fixed-trajectory OCP method (dash-dot), and the fixed-trajectory apex-finding method (dashed).

accelerating) and cornering, increasing the roll stiffness ratio is beneficial, and higher deceleration (or acceleration) can be achieved. Indeed, in such condition the rear tyres saturates, and thus minimizing the load transfer on the rear axle is beneficial for improving the performance, i.e. the g-g area. The optimal value of the roll stiffness ratio is the best trade-off between these two effects.

In most of the practical cases, the race line is available for a certain configuration only. The fixed-trajectory methods allow us to investigate the effect of a given parameter, together with the g-g diagrams calculated with different values of such parameter, while still employing the same predetermined trajectory. As an example of application, the race line resulting from the baseline vehicle optimal lap (with the baseline friction) is selected (Section 4.1.1). The fixed-trajectory OCP and the apex-finding method (Fig. 9) are employed on such trajectory, together with the g-g surfaces obtained for low friction conditions, at different values of the roll stiffness ratio ξ. The lap time is then compared against the lap time obtained with the free-trajectory OCP optimisation for low adher-

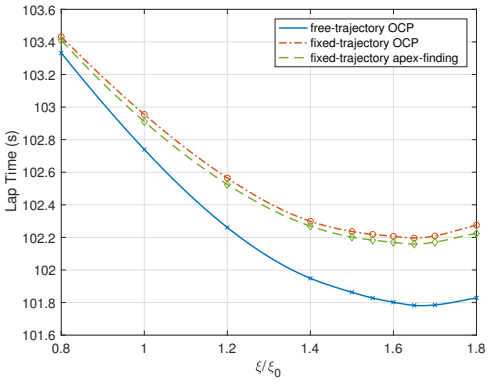

Figure 9.: Lap time versus the normalised roll-ratio parameter ξ/ξ_0, using the low-friction free-trajectory OCP method (solid), the fixed-trajectory OCP method (dash-dot) computed on the baseline friction race line (with low-friction g-g), and the fixed-trajectory apex-finding method (dashed) computed on the baseline friction race line (with low-friction g-g).

ence conditions (Fig. 9). The lap times obtained with the fixed-trajectory methods are higher, since the race line used (which is optimal for baseline-friction condition) is not the optimal one for the g-g surfaces selected (which relate to the low-friction condition). However, when it comes to the parameter optimisation, the fixed-trajectory methods give the same optimal parameter value as the free-trajectory methods, although they are run on a suboptimal trajectory. This need not be always the case.

4.1.5. Remarks on problem size

With the current implementation, the computation time of the free-trajectory OCP is about three times the computation time of the fixed-trajectory OCP, while the computation time of the fixed-trajectory apex-finding method is about one-and-a-half the computation time of the fixed trajectory OCP. However, the fixed-trajectory methods require some pre-processing work in order to obtain a suitable race line (either experimentally or numerically, e.g. using a free-trajectory optimisation).

The computational effort of the three methods employed can be compared through the inspection of the number of equations that have to be solved in the baseline configuration, and the number of related solver iterations. The free-trajectory OCP needs to solve 328 equations (state equations plus constraints) with the initial mesh grid, which consists of 41 mesh points (in the range 25-100 m). In the final mesh grid, the number of mesh points is 1478 and the number of equations raises to 11824. The total number of equations solved after the 10 mesh-refinement steps is 83952, while the total number of iterations performed by IPOPT is 2884. The fixed-trajectory OCP needs to solve 123 equations with the initial mesh grid, which consists of 41 mesh points. In the final mesh grid the number of mesh points is 446 and the number of equations to solve is 1338. The total number of equations solved after the 7 mesh-refinement steps is 6270, while the total number of iterations performed by IPOPT is 7558. Finally, the apex-finding method has a constant number of 26596 mesh points (since there is no mesh refinement) and as many equations. The total number of iterations performed by its root-finding solver is 102373.

4.2. *Motorcycle model*

The g-g diagram of the motorcycle is computed employing the essential model reported in [35], which is extended to include the drag force and the engine power limit. Both the suspensions and the steer angle are neglected. As in the car model, the yaw rate Ω is

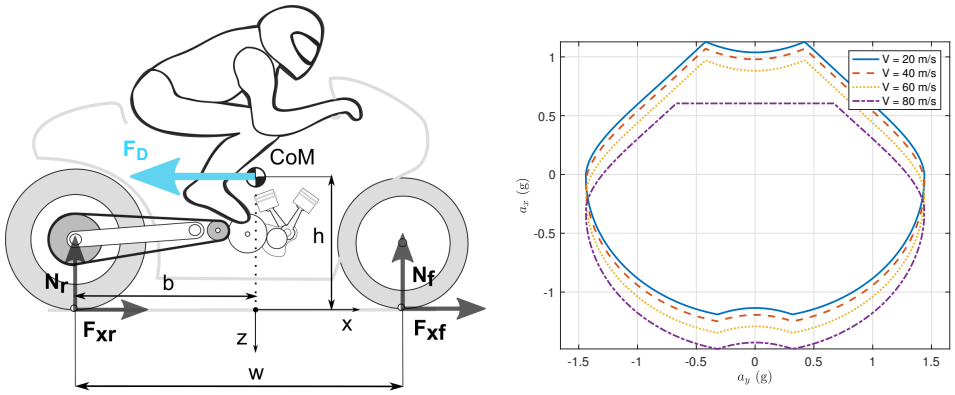

Figure 10.: Motorcycle model (left) and related g-g diagrams at different speeds (right).

related to the lateral acceleration a_y and the velocity V by $\Omega = a_y/V$. In order to obtain a compact formulation, it is further assumed that the vehicle sideslip angle is small, that the motorcycle is symmetric with respect to the x-z plane (i.e. $I_{xy} = I_{yz} = 0$), that the cross moment of inertia I_{xz} is negligible, and that $I_y \approx I_z$. The benefit of such model is that a compact formulation is obtained, while retaining motorcycle peculiarities such as roll-dependent stoppie and wheelie limits.

The steady-state equations of motion are:

$$ma_x = F_{xr} + F_{xf} - F_D \tag{44}$$

$$ma_y = F_{yr} + F_{yf} \tag{45}$$

$$mg = N_r + N_f \tag{46}$$

$$ma_y h\cos\phi = mgh\sin\phi \tag{47}$$

$$ma_x h\cos\phi = bN_r - (w-b)N_f - F_D h_a\cos\phi \tag{48}$$

$$ma_x h\sin\phi = bF_{yr} - (w-b)F_{yf} - F_D h_a\sin\phi, \tag{49}$$

where the first three equations represent the balance of forces along the longitudinal, lateral and vertical axes, while the latter three equations represent the moment balance around the roll, pitch and yaw axes. The meaning of the model parameters and values used in the simulations are reported in Tab. 2, while the force and the axes convention are depicted in Fig. 10 (left). The lateral forces are represented by F_{yr} and F_{yf} for the rear and front tyre respectively, while the roll angle ϕ is measured from the vertical plane x-z. During braking, the longitudinal forces F_{xr} and F_{xf} are related by

$$\gamma = \frac{F_{xf}}{F_{xr}}, \tag{50}$$

where the brake ratio γ (compare with (39) where γ was defined for cars) is zero during acceleration and is determined by the rider in braking. The seven steady-state equations (44)-(50) can be solved analytically for $\phi, N_r, N_f, F_{xr}, F_{xf}, F_{yr}, F_{yf}$. Such solution will be used to derive the g-g boundaries.

The aerodynamics force is applied on the center of pressure, and is given by

$$F_D = \frac{1}{2}\rho_a C_D A V^2. \tag{51}$$

The coupling between longitudinal and lateral forces is included through friction ellipses, which (at the limit of friction) are given by

$$\left(\frac{F_{xr}/N_r}{\mu_x}\right)^2 + \left(\frac{F_{yr}/N_r}{\mu_y}\right)^2 = 1, \tag{52}$$

$$\left(\frac{F_{xf}/N_f}{\mu_x}\right)^2 + \left(\frac{F_{yf}/N_f}{\mu_y}\right)^2 = 1, \tag{53}$$

where μ_x and μ_y are the longitudinal and lateral friction coefficients respectively.

The maximum acceleration, i.e. the upper boundary of the g-g map, is obtained when introducing the analytical solution of the steady-state equations (44)-(50) into the rear

friction ellipse (52), to give

$$\left(\frac{w(ma_x + F_D)\sqrt{a_y^2 + g^2}}{g((w-b)m\sqrt{a_y^2 + g^2} + ma_x h + F_D h_a)} \right)^2 \frac{1}{\mu_x^2} + \left(\frac{a_y}{g} \right)^2 \frac{1}{\mu_y^2} = 1, \tag{54}$$

which can be solved for the longitudinal acceleration a_x at different lateral accelerations a_y, using a standard root-finding solver.

Since the maximum engine power $P_{\max}$ is given, the longitudinal force balance (44) can be used to compute the related acceleration limit

$$a_x = \frac{P_{\max}}{mV} - \frac{F_D}{m}. \tag{55}$$

Differently from cars, the front tyre of a motorcycle can lift the road during acceleration (wheelie condition). The related acceleration limit is obtained from the condition $N_f = 0$, which can be solved analytically to give

$$a_x = \frac{b\sqrt{a_y^2 + g^2}}{h} - \frac{F_D h_a}{mh}. \tag{56}$$

In order to compute the minimum deceleration, it is assumed that the rider applies an optimal brake ratio: this condition occurs when the front and rear tyres are engaged equally, i.e. $F_{xr}/N_r = F_{xf}/N_f$. The condition (52)=(53) gives the following (longitudinal- and lateral-acceleration dependent) optimal brake ratio

$$\gamma_{opt} = \frac{mb\sqrt{a_y^2 + g^2} - ma_x h - F_D h_a}{m(w-b)\sqrt{a_y^2 + g^2} + ma_x h + F_D h_a}. \tag{57}$$

When introducing the analytical solution of the steady-state equations (44)-(50), together with (57) into either the front or rear friction ellipse (53), one obtains

$$-a_x = g\mu_x \sqrt{1 - \left(\frac{a_y}{g} \right)^2 \frac{1}{\mu_y^2}} + \frac{F_D}{m}. \tag{58}$$

Again, differently from cars, the rear tyre of a motorcycle can lift the road while braking (stoppie condition). The related deceleration limit is obtained from the condition $N_r = 0$, which can be solved analytically to give

$$-a_x = \frac{(w-b)\sqrt{a_y^2 + g^2}}{h} - \frac{F_D h_a}{mh}. \tag{59}$$

In sum, the g-g diagram is obtained by the envelope of (54), (55), (56), (58), and (59). The g-g diagram of the motorcycle, obtained with the dataset in Tab. 2, is shown in Fig. 10 (right) at different speeds. The main differences with respect to the car g-g diagram (Fig. 1) are the 'dips' related to wheelie and stoppie, which limit the motorcycle performance in straight motion and small lateral acceleration.

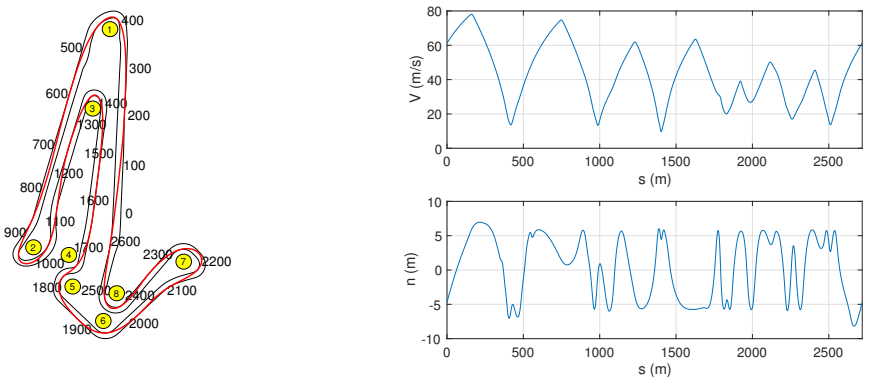

Figure 11.: Baseline motorcycle configuration. Trajectory on the Adria International Raceway (left), with corner numbers and distance (curvilinear abscissa s) from the start/finish line. Speed V (top-right) and lateral position n (bottom-right) along the curvilinear coordinate.

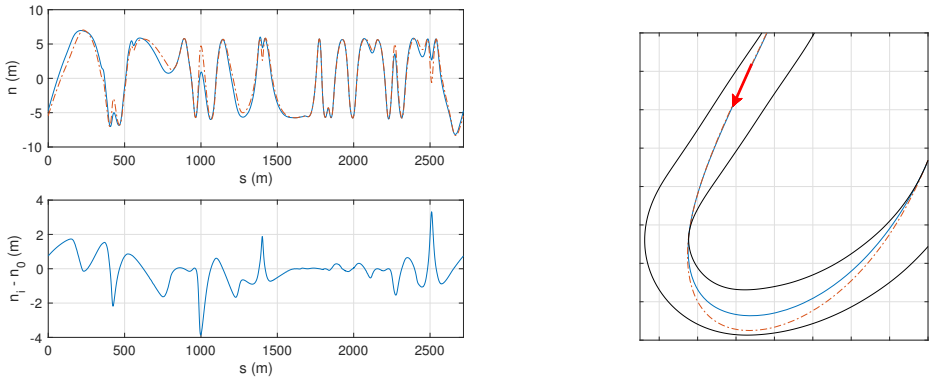

Figure 12.: Lateral position n for car and motorcycle (top-left) and lateral position difference with respect to the car baseline (bottom-left). Magnified view of turn 2, together with the race lines (right). Baseline car (dot-dash), baseline motorcycle (solid).

4.2.1. Baseline simulation

The free-trajectory OCP of the race motorcycle gives a minimum lap time of 72.519 s. The parameters used are reported in Tab. 2. The race line along the Adria International Raceway is shown in Fig. 11 (left).The speed profile and the lateral displacement with respect to the centre line are shown in Fig. 11 (right). The vehicle reaches a top speed of 78 m/s in the home straight, while the minimum speed of 9.5 m/s is reached in turn 3.

Similarly to the race car scenario, even in the case of the motorcycle the lap time obtained with the fixed-trajectory methods (either OCP or apex-finding) almost coincides with the lap time of the free-trajectory OCP (difference around 0.02%), as long as the predefined trajectory is the optimal race line obtained from the free-trajectory OCP.

As for the race car, the problems are discretised using differently spaced mesh points along the track centre line. The mesh points of the OCP solutions are unevenly spaced (in the range 0.1-10 m), and result from the solution of the optimisation problem, while the apex-finding approach has a 0.1 m equally spaced mesh. See Sec. 4.2.2 for further details on the computation implications of the different methods.

4.2.2. Remarks on problem size

With the current implementation, the computation time of the free-trajectory OCP is similar to the computation time of the fixed-trajectory OCP, while the computation time of the fixed-trajectory apex-finding method is about three-and-a-half the computation time of the fixed-trajectory OCP. However, the fixed-trajectory methods require some pre-processing work in order to obtain a suitable race line.

As in the case of the car model, the computational effort of the three methods employed can be compared through the inspection of the number of equations that have to be solved in the baseline configuration, and the number of related solver iterations. The free-trajectory OCP needs to solve 328 equations (state equations plus constraints) with the initial mesh grid, which consists of 41 mesh points – this is identical to the car problem. In the final mesh grid, the number of mesh points is 1478 and the number of equations raises to 11704. The total number of equations solved after the 10 mesh-refinement steps is 82696, while the total number of iterations performed by IPOPT is 512 – the number of equations is close to that of the car problem, the number of mesh steps is the same, while the number of iterations is smaller. The fixed-trajectory OCP needs to solve 123 equations with the initial mesh grid, which consists of 41 mesh points – again this is identical to the car problem. In the final mesh grid, the number of mesh points is 446 and the number of equations to solve is 1386. The total number of equations solved after the 8 mesh-refinement steps is 7731, while the total number of iterations performed by IPOPT is 7434 – the numbers are close to those of the car problem. Finally, the size of the apex-finding method is identical to the case of the race car, i.e. 26596 mesh points, and the number solver iterations is close (100943).

4.2.3. Car vs. motorcycle simulations

The friction coefficients of the motorcycle μ_x and μ_y have been chosen in order to have the maximum lateral acceleration and g-g diagram area similar to those of the race car at low speeds (indeed at high speeds the aerodynamics of the race car becomes a dominant factor); see Fig. 13 where the g-g diagrams are compared at 20 m/s and 80 m/s. The motorcycle g-g map includes the distinctive effects of wheelie and stoppie during acceleration and braking. This behaviour is typical for motorcycles and limits the maximum and minimum acceleration available (see Sec. 4.2). In spite of that, the motorcycle is capable of reaching higher accelerations, because of the larger height-to-wheelbase ratio (see Fig. 13 left), lower drag area and higher power-to-mass ratio (see

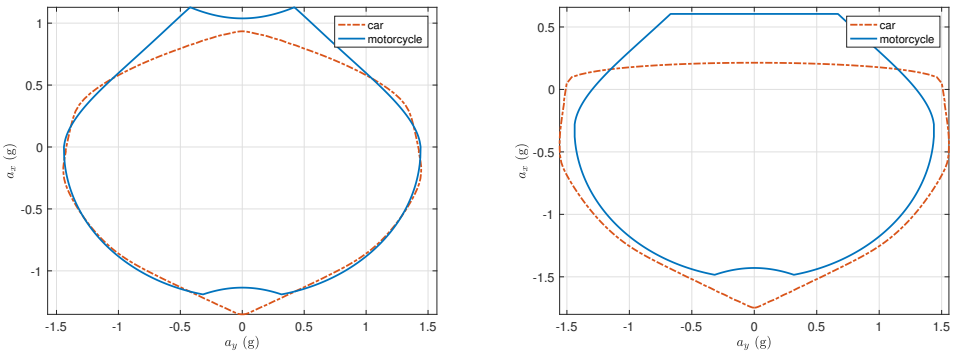

Figure 13.: Motorcycle (solid) and car (dash-dot) g-g diagram at $V = 20$ m/s (left) and at $V = 80$ m/s (right).

Fig. 13 right). On the other hand, the downforces allow the car to potentially reach higher lateral accelerations (see Fig. 13 right). However, the selected track does not include high speed corners to exploit such advantage. For this reason the motorcycle reaches a top speed 10 m/s higher than the car, while, at turn 3, the minimum speed reached by the motorcycle is 1.4 m/s higher. Therefore the lap time is 4% lower for the motorcycle.

The two vehicles also employ different race lines, in particular during tight corners (Fig. 12). At turn 1 (300-500 m), the motorcycle starts the cornering manoeuvre with a larger race line, goes tighter to the inner kerb at the corner apex, and exits with a larger trajectory. At turn 2 (900-1100 m), turn 3 (1300-1500 m) and turn 8 (2100-2300 m) the behaviour is similar.

5. Conclusion

A method for computing the minimum lap time of road vehicles, together with the related optimal race line, has been presented. The method builds upon the g-g-speed surfaces that can either be derived experimentally (from track data) or numerically (from QSS models). The key features of the proposed approach can be summarised as follows: the computation of the optimal race line is allowed without involving a full-dynamic vehicle model (QSS models suffice); the method is suitable for application both to cars and motorcycles (as shown by the two examples included); all the model complexity is confined to the g-g-surfaces (i.e. the model complexity does not affect the complexity of the resulting OCP problem). Moreover, with the current implementation, the computation time of the free-trajectory approach lies between one and three times the computation time of the fixed-trajectory approaches. In this work, the effect of the tyre-road friction, brake ratio, and roll-stiffness ratio on the optimal trajectory of a race car has been discussed. The effect of the fixed-trajectory assumption has been also investigated in the case of the optimisation of the roll-stiffness ratio. The comparison between the key features of the g-g diagrams of cars and motorcycles has been also included, as well as the comparison between the related optimal trajectories.

References

[1] Scherenberg H. Mercedes-benz racing design and cars experience. SAE Technical Paper; 1958. Report No.: 1958-01-01.
[2] Metz D, Williams D. Near time-optimal control of racing vehicles. Automatica. 1989;25(6):841–857.
[3] Gadola M, Vetturi D, Cambiaghi D, Manzo L. A tool for lap time simulation. SAE Technical Paper; 1996. Report No.: 1996-12-01.
[4] Siegler B, Deakin A, Crolla D. Lap time simulation: Comparison of steady state, quasi-static and transient recing car cornering stategies. In: of Automotive Engineers S, editor. 2000 SAE Motorsports Engineering conference amd Exposition; paper 2000–01-3563. SAE International; 2000. p. 9.
[5] Brayshaw D, Harrison M. A quasi steady state approach to race car lap simulation in order to understand the effects of racing line and centre of gravity location. Proceedings of the Institution of Mechanical Engineers, Part D: Journal of Automobile Engineering. 2005;219(6):725–739.
[6] Brayshaw D, Harrison M. Use of numerical optimization to determine the effect of the roll stiffness distribution on race car performance. Proceedings of the Institution of Mechanical Engineers, Part D: Journal of Automobile Engineering. 2005;219(10):1141–1151.
[7] Savaresi SM, Spelta C, Ciotti D, Sofia M, Rosignoli E, Bina E. Virtual selection of the optimal gear-set in a race car. International Journal of Vehicle Systems Modelling and Testing. 2008;3(1-2):47–67.
[8] Kelly DP, Sharp RS. Time-optimal control of the race car: influence of a thermodynamic tyre model. Vehicle System Dynamics. 2012;50(4):641–662.

[9] Völkl T, Muehlmeier M, Winner H. Extended steady state lap time simulation for analyzing transient vehicle behavior. SAE International Journal of Passenger Cars-Mechanical Systems. 2013;:283–292.
[10] Tremlett A, Assadian F, Purdy D, Vaughan N, Moore A, Halley M. Quasi-steady-state linearisation of the racing vehicle acceleration envelope: a limited slip differential example. Vehicle System Dynamics. 2014;52(11):1416–1442.
[11] Hendrikx J, Meijlink T, Kriens R. Application of optimal control theory to inverse simulation of car handling. Vehicle System Dynamics. 1996;26(6):449–461.
[12] Cossalter V, Da Lio M, Lot R, Fabbri L. A general method for the evaluation of vehicle manoeuvrability with special emphasis on motorcycles. Vehicle system dynamics. 1999;31(2):113–135.
[13] Casanova D, Sharp RS, Symonds P. Minimum time manoeuvring: The significance of yaw inertia. Vehicle system dynamics. 2000;34(2):77–115.
[14] Casanova D. On minimum time vehicle manoeuvring: The theoretical optimal lap [dissertation]. School of Engineering, Cranfield University; 2000.
[15] Bertolazzi E, Biral F, Da Lio M. Symbolic-numeric efficient solution of optimal control problems for multibody systems. Journal of computational and applied mathematics. 2006;185(2):404–421.
[16] Kelly DP. Lap time simulation with transient vehicle and tyre dynamics [dissertation]. Cranfield University; 2008.
[17] Bobbo S, Cossalter V, Massaro M, Peretto M. Application of the optimal maneuver methodî for enhancing racing motorcycle performance. SAE International Journal of Passenger Cars-Mechanical Systems. 2009;1(1):1311–1318.
[18] Tavernini D, Massaro M, Velenis E, Katzourakis D, Lot R. Minimum time cornering: The effect of road surface and car transmission layout. Vehicle System Dynamics. 2013;51(10):1533–1547.
[19] Tavernini D, Velenis E, Lot R, Massaro M. The optimality of the handbrake cornering technique. Journal of Dynamic Systems, Measurement, and Control. 2014;136(4).
[20] Perantoni G, Limebeer DJ. Optimal control for a formula one car with variable parameters. Vehicle System Dynamics. 2014;52(5):653–678.
[21] Limebeer DJN, Perantoni G, Rao AV. Optimal control of formula one car energy recovery systems. International Journal of Control. 2014;87(10):2065–2080.
[22] Masouleh MI, Limebeer DJN. Optimizing the aero-suspension interactions in a formula one car. IEEE Transactions on Control Systems Technology. 2016 May;24(3):912–927.
[23] Tremlett A, Massaro M, Purdy D, Velenis E, Assadian F, Moore A, Halley M. Optimal control of motorsport differentials. Vehicle System Dynamics. 2015;53(12):1772–1794.
[24] Tremlett A, Limebeer D. Optimal tyre usage for a formula one car. Vehicle System Dynamics. 2016; 54(10):1448–1473.
[25] Dal Bianco N, Lot R, Gadola M. Minimum time optimal control simulation of a gp2 race car. Proceedings of the Institution of Mechanical Engineers, Part D: Journal of Automobile Engineering. 2017;232(9):1180–1195.
[26] Bianco ND, Bertolazzi E, Biral F, Massaro M. Comparison of direct and indirect methods for minimum lap time optimal control problems. Vehicle System Dynamics. 2018;0(0):1–32.
[27] Limebeer DJN, Massaro M. Dynamics and optimal control of road vehicles. Oxford University Press; 2018.
[28] Patterson MA, Rao AV. GPOPS-II: A MATLAB software for solving multiple-phase optimal control problems using hp-adaptive gaussian quadrature collocation methods and sparse nonlinear programming. ACM Transactions on Mathematical Software (TOMS). 2014;41(1):1.
[29] Weinstein MJ, Rao AV. Algorithm 984: Adigator, a toolbox for the algorithmic differentiation of mathematical functions in matlab using source transformation via operator overloading. ACM Trans Math Softw. 2017 Aug;44(2):21:1–21:25.
[30] Gillespie TD. Fundamentals of vehicle dynamics. SAE International; 1992.
[31] Jazar RN. Vehicle dynamics: theory and application. Springer; 2017.
[32] Pacejka H, Besselink I. Tire and vehicle dynamics. Elsevier Science; 2012.
[33] Wächter A, Biegler LT. On the implementation of an interior-point filter line-search algorithm for large-scale nonlinear programming. Mathematical Programming. 2006 Mar;106(1):25–57.
[34] Edelmann J, Plöchl M. Handling characteristics and stability of the steady-state powerslide motion of an automobile. Regular and Chaotic Dynamics. 2009 Dec;14(6):682.
[35] Biral F, Lot R. An interpretative model of g-g diagrams of racing motorcycle. In: Proceedings of the 3rd ICMEM International Conference on Mechanical Engineering and Mechanics; 2009.

Table 1.: Baseline car parameters.

Symbol	**Description**	**Value**
g	gravity	$9.81\,\mathrm{m/s^2}$
ρ_a	air density	$1.20\,\mathrm{kg/m^3}$
m	mass	$1300\,\mathrm{kg}$
h	height of center of mass	$0.330\,\mathrm{m}$
w	wheelbase	$2.900\,\mathrm{m}$
b	longitudinal distance of the center of mass	$1.535\,\mathrm{m}$
a	$w - b$	$1.365\,\mathrm{m}$
I_z	yaw inertia	$1700\,\mathrm{kgm^2}$
T	vehicle track	$2.016\,\mathrm{m}$
γ_0	brake ratio F_{xf}/F_{xr}	1.13
ξ_0	roll stiffness ratio	0.53
$C_D A$	drag area coefficient	$0.65\,\mathrm{m^2}$
$C_{Lf} A$	front lift area coefficient	$0.15\,\mathrm{m^2}$
$C_{Lr} A$	rear lift area coefficient	$0.35\,\mathrm{m^2}$
$P_{\max}$	maximum power	$415\,\mathrm{kW}$
$\delta_{\max}$	maximum wheel steer angle	$20\,\mathrm{deg}$
$pCx1$	longitudinal shape factor	1.6935
$pDx1$	max longitudinal friction coefficient	1.8757
$pDx2$	longitudinal friction load dependency factor	-0.127
$pEx1$	longitudinal curvature factor	0.07708
$pKx1$	max longitudinal stiffness coefficient	30.5
$pKx3$	max longitudinal stiffness coefficient	0.2766
λ_{μ_x}	longitudinal scaling factor	0.93
$pCy1$	lateral shape factor	1.733
$pDy1$	max lateral friction coefficient	1.8217
$pDy2$	lateral friction load dependency factor	-0.4388
$pEy1$	lateral curvature factor	0.29446
$pKy1$	max cornering stiffness coefficient	44.2
$pKy2$	max cornering stiffness coefficient	2.5977
λ_{μ_y}	lateral scaling factor	0.84
N_0	nominal load (where $df_z = 0$)	$3500\,\mathrm{N}$

Table 2.: Motorcycle (plus rider) parameters.

Symbol	**Description**	**Value**
g	gravity	$9.81\,\mathrm{m/s^2}$
ρ_a	air density	$1.20\,\mathrm{kg/m^3}$
m	mass	$250\,\mathrm{kg}$
h	height of center of mass	$0.69\,\mathrm{m}$
h_a	height of center of pressure	$0.69\,\mathrm{m}$
w	wheelbase	$1.50\,\mathrm{m}$
b	longitudinal distance of the center of mass	$0.73\,\mathrm{m}$
$C_D A$	drag area coefficient	$0.20\,\mathrm{m^2}$
$P_{\max}$	maximum power	$180\,\mathrm{kW}$
μ_x	longitudinal friction coefficient	1.2
μ_y	lateral friction coefficient	1.44